AFRL-RD-PS-
TP-2021-0020

OPTIMIZATION OF MICROWAVE EMISSION FROM LASER FILAMENTATION WITH A MACHINE LEARNING ALGORITHM IN AIR

Alexander Englesbe, et al.

8 July 2021

Technical Paper

AIR FORCE RESEARCH LABORATORY
Directed Energy Directorate
3550 Aberdeen Ave SE
AIR FORCE MATERIEL COMMAND
KIRTLAND AIR FORCE BASE, NM 87117-5776

NOTICE AND SIGNATURE PAGE

Using Government drawings, specifications, or other data included in this document for any purpose other than Government procurement does not in any way obligate the U.S. Government. The fact that the Government formulated or supplied the drawings, specifications, or other data, does not license the holder or any other person or corporation; or convey any rights or permission to manufacture, use, or sell any patented invention that may relate to them.

This report was cleared for public release by the AFMC Public Affairs Office and is available to the general public, including foreign nationals. Copies may be obtained from the Defense Technical Information Center (DTIC) (http://www.dtic.mil).

AFRL-RD-PS-TP-2021-0020 HAS BEEN REVIEWED AND IS APPROVED FOR PUBLICATION IN ACCORDANCE WITH ASSIGNED DISTRIBUTION STATEMENT.

SCHMITT-SODY.ANDREAS.1292923151 Digitally signed by SCHMITT-SODY.ANDREAS.1292923151 Date: 2021.07.12 12:04:40 -06'00'

Andreas Schmitt-Sody, DR-III
Senior Research Engineer, AFRL/RDHP

LANGDON.STEPHEN.L.1232187065 Digitally signed by LANGDON.STEPHEN.L.1232187065 Date: 2021.07.12 12:15:09 -06'00'

Stephen Langdon, DR-III
Branch Chief, AFRL/RDHP

This report is published in the interest of scientific and technical information exchange, and its publication does not constitute the Government's approval or disapproval of its ideas or findings.

REPORT DOCUMENTATION PAGE

Form Approved
OMB No. 0704-0188

1. REPORT DATE *(DD-MM-YYYY)*	**2. REPORT TYPE**	**3. DATES COVERED** *(From - To)*
08-07-2021	Technical Paper	N/A

4. TITLE AND SUBTITLE

Optimization of Microwave Emission from Laser Filamentation with a Machine Learning Algorithm

5a. CONTRACT NUMBER

FA9451-20-F-0001

5b. GRANT NUMBER

5c. PROGRAM ELEMENT NUMBER

6. **AUTHOR(S)**

Alexander Englesbe
Jinpu Lin
John Nees
Karl Krushelnick
Adrian Lucero
Andreas Schmitt-Sody

5d. PROJECT NUMBER

5e. TASK NUMBER

5f. WORK UNIT NUMBER

D0G9

7. PERFORMING ORGANIZATION NAME(S) AND ADDRESS(ES)

Air Force Research Laboratory 3550 Aberdeen Ave SE Kirtland AFB, NM 87117-5776
University of Michigan, 2200 Bonisteel Blvd., Ann Arbor, MI, 48109
Naval Research Laboratory,4555 Overlook Ave., Washington, DC 20375

8. PERFORMING ORGANIZATION REPORT NUMBER

9. SPONSORING / MONITORING AGENCY NAME(S) AND ADDRESS(ES)

Air Force Research Laboratory
3550 Aberdeen Ave. SE
Kirtland AFB, NM 87117-5776

10. SPONSOR/MONITOR'S ACRONYM(S)

RDHP

11. SPONSOR/MONITOR'S REPORT NUMBER(S) AFRL-RD-PS-TP-2021-0020

12. DISTRIBUTION / AVAILABILITY STATEMENT

DISTRIBUTION A: Approved for Public Release: Distribution Unlimited. AFMC-2021-0873

13. SUPPLEMENTARY NOTES

Published in Applied Optics Vol. 60 No. 25

14. ABSTRACT

We demonstrate that is it possible to optimize the yield of microwave radiation from plasmas generated by laser filamentation in atmosphere through manipulation of the laser wavefront. A genetic algorithm controls a deformable mirror that reconfigures the wavefront using the microwave waveform amplitude as feedback. Optimization runs performed as a function of air pressure show that the genetic algorithm can double the microwave field strength relative to when the mirror surface is flat. An increase in the volume and brightness of the plasma fluorescence accompanies the increase in microwave radiation, implying an improvement in the laser beam intensity profile through the filamentation region due to the optimized wavefront.

15. SUBJECT TERMS

Laser filamentation, high intensity lasers, laser plasma, laser plasma dynamics,

16. SECURITY CLASSIFICATION OF:			**17. LIMITATION OF ABSTRACT**	**18. NUMBER OF PAGES**	**19a. NAME OF RESPONSIBLE PERSON** A. Schmitt-Sody
a. REPORT	**b. ABSTRACT**	**c. THIS PAGE**			**19b. TELEPHONE NUMBER** *(include area code)*
UNCLASSIFIED	UNCLASSIFIED	UNCLASSIFIED	SAR	35	

This page left intentionally blank

Optimization of Microwave Emission from Laser Filamentation with a Machine Learning Algorithm

Alexander Englesbe

U.S. Naval Research Laboratory, 4555 Overlook Ave. SW, Washington, DC, 20375

Jinpu Lin, John Nees, and Karl Krushelnick

Gérard Mourou Center for Ultrafast Optical Science,

University of Michigan, 2200 Bonisteel Blvd., Ann Arbor, MI, 48109

Adrian Lucero and Andreas Schmitt-Sody

U.S. Air Force Research Laboratory,

3550 Aberdeen Ave SE, Kirtland AFB, NM, 87117

Abstract

We demonstrate that is it possible to optimize the yield of microwave radiation from plasmas generated by laser filamentation in atmosphere through manipulation of the laser wavefront. A genetic algorithm controls a deformable mirror that reconfigures the wavefront using the microwave waveform amplitude as feedback. Optimization runs performed as a function of air pressure show that the genetic algorithm can double the microwave field strength relative to when the mirror surface is flat. An increase in the volume and brightness of the plasma fluorescence accompanies the increase in microwave radiation, implying an improvement in the laser beam intensity profile through the filamentation region due to the optimized wavefront.

I. INTRODUCTION

In laser filamentation, a nonlinear process that balances Kerr self-focusing with plasma defocusing and diffraction [1, 2], small spatial and temporal fluctuations in the laser field precipitate a large range of different behaviors in its propagation [3–9]. This has led to broad investigation of filamentation control schemes spanning over a decade of research. Possible control approaches have leveraged all aspects of the laser field, including shaping the transverse beam profiles with amplitude [10, 11] and phase masks [12–15], and coherent synthesis of fields in the temporal and spectral domains [16–18]. The idea is that with sufficient study, it is possible that correct manipulation of the initial laser pulse will enable robust engineering of individual filaments, or arrays of multiple filaments that might even be controlled in real time in order to optimize a given laser-matter interaction. The impression arises from this body of work that a given control scheme is suited to a single purpose or application, and that a universal method for filament control has yet to emerge.

One strategy for attempting filament control that has shown promise in multiple applications is to use an adaptive optical element with may degrees of freedom, such as a spatial light modulator (SLM) [19] or deformable mirror (DM) [20] to precisely structure the initial wavefronts (the transverse spatial phase) of the pulses at the output aperture of the laser. SLMs can be undesirable for use with high intensity ultrashort pulses owing to low damage thresholds, however they typically have a larger number of pixels than DMs have actuators, which affords a significantly finer degree of control over the spatial phase. Given the large parameter space available to adaptive optical elements, the challenge becomes identifying the correct wavefront that achieves the desired outcome. Indeed prior studies have reduced this parameter space by imposing selected modes on the wavefronts and grouping DM actuators [21, 22] or SLM pixels [23] together based on predictions of the outcome.

One way to avoid the reduction and use all the available degrees of freedom is to borrow techniques from machine learning to perform a heuristic search, instead of one that is inherently based on first principles. This approach has enabled optimization of filamentation and filament interactions in several scenarios [24–28], and also other high intensity laser-matter interactions such as laser wakefield acceleration of electrons [29–31].

We use a DM controlled by a genetic algorithm (GA) to impose iteratively refined distortions to the spatial phase of the laser pulses that optimize the generation of broadband

microwave radiation from the plasma generated in the filament wake. A GA is a common machine learning tool that executes many repetitive semi-random searches to converge to a solution using biologically inspired operators [32]. GAs can be useful tools when performing an optimization over a large parameter space in which the correspondence between the attributes of the input and their effect on the output cannot be easily predicted.

We measure the peak amplitude of voltage waveforms from radiation received in the far field, and feed that amplitude value back to the GA to perform the optimization. The microwave radiation arises from the residual energy of the electrons imparted by the ionizing laser field [33, 34]. As the laser pulse filaments and produces a plasma column, the hottest electrons in the electron energy distribution located at the surface of the column thermally expand beyond the plasma boundary producing a transient radial electric field. As the pulse propagates, the previously ionized electrons will have expanded to a greater radial extent than the newly ionized electrons, creating a net charge distribution with a conical profile. The longitudinal asymmetry of the cone stimulates a surface current along the plasma column initiated coherently behind the laser pulse. The current builds up an electromagnetic field as it traverses the plasma, which detaches when the plasma terminates, and radiates as a radially polarized broadband electromagnetic pulse. This mechanism is distinct from that which produces terahertz radiation in filament plasmas [35, 36].

Collisions between the electrons and heavy neutral species impede their conical expansion, which ultimately regulates the longitudinal current producing the radiation. We can vary the baseline amount of microwave radiation by reducing the air pressure. A strong inverse relationship between the microwave yield and air pressure has been documented before [37, 38], and in these experiments we observe that the efficacy of the GA optimization itself depends on the air pressure. The work originated out of the desire to fully characterize the radiation in the RF and microwave frequency regime to better understand the laser-plasma interaction. We see utility in the RF as a tool to analyze the generated plasma. As well as using the emitted RF for broadband single shot microwave spectroscopy.

It is not guaranteed that the shape of the wavefront can significantly influence the microwave radiation caused by the laser pulses. While small wavefront changes applied by the mirror may be amplified by the nonlinear propagation, there are several sequential physical processes (nonlinear propagation, ionization of the air, and formation of plasma currents) that must occur for the wavefront manipulation to translate to changes in the microwave

yield. Strong field ionization depends on the instantaneous value of the laser electric field, so reshaping the wavefront can effect a degree of change in the size and properties of the plasma. This is how we expect the deformable mirror can optimize the microwave yield. We observe that the GA is able to find DM configurations that enhance the electric field strength of the microwave radiation by up to a factor of 2 over the frequency range of the measurements.

The increase in the electric field due to the GA is uniform across the frequency range of our receiver, and is insensitive to the receiver position during the optimization. This is unusual only because the spatial emission pattern of the microwaves is conical in shape, and spectrally stratified, with higher frequency components predominantly radiated near to the laser axis [37]. Even though the microwave enhancement is repeatable, we find that the GA does not converge to the same mirror shape for each case of air pressure or receiver position we test, although it is possible that there are some similarities among the collection of mirror shapes. Finally, images of the plasma fluorescence and the laser intensity profile before and after the optimizations imply that the GA improves the beam mode content, since larger and more intensely fluorescing plasmas and a more circular transverse intensity profile result from optimizing the microwave yield.

II. EXPERIMENTAL METHODS

A. Laser System and Optical Setup

The experimental setup, shown in Fig. 1 is similar to that of Refs. [24, 37, 38]. We used the λ^3 laser [39] in the Center for Ultrafast Optical Science at the University of Michigan for the experiments. It is a high average power Ti:sapphire system that delivers pulses at $\lambda = 800$ nm with a FWHM pulse duration of about 35 fs. The pulse repetition rate is 480 Hz, and the energy per pulse is held constant at 3.7 ± 0.5 mJ (the average power is 1.8 ± 0.2 W). The peak power corresponds to about $10P_{cr}$ for 800 nm light in atmosphere. After reflecting from the deformable mirror, a concave mirror focuses the pulses ($f = 2$ m, f-number is $f/40$). The region where the plasma forms is contained inside a quartz gas cell capped with thin windows. A diaphragm pump connected to the cell allows the pressure to vary from atmosphere to 1 Torr. At lower pressures, the nonlinear contribution decreases and the

pulse will not forgo filmenatioan, but rather non-linear propagation with plasma formation. We expect that at pressures below 76 Torr no filamentation to occur. While reducing the pressure, the pulse propagation will evolve from the multi-filament regime to single filament to non-linear focusing and plasma formation close to the focal region. For simplicity of writing we refer to filamention throughout this paper for all of the scenarios. Additionally, we used a Stanford Computer Optics 4 Quik E intensified charged coupled device (ICCD) camera with 16-bit dynamic range to record images of the plasma fluorescence and estimate its length and width.

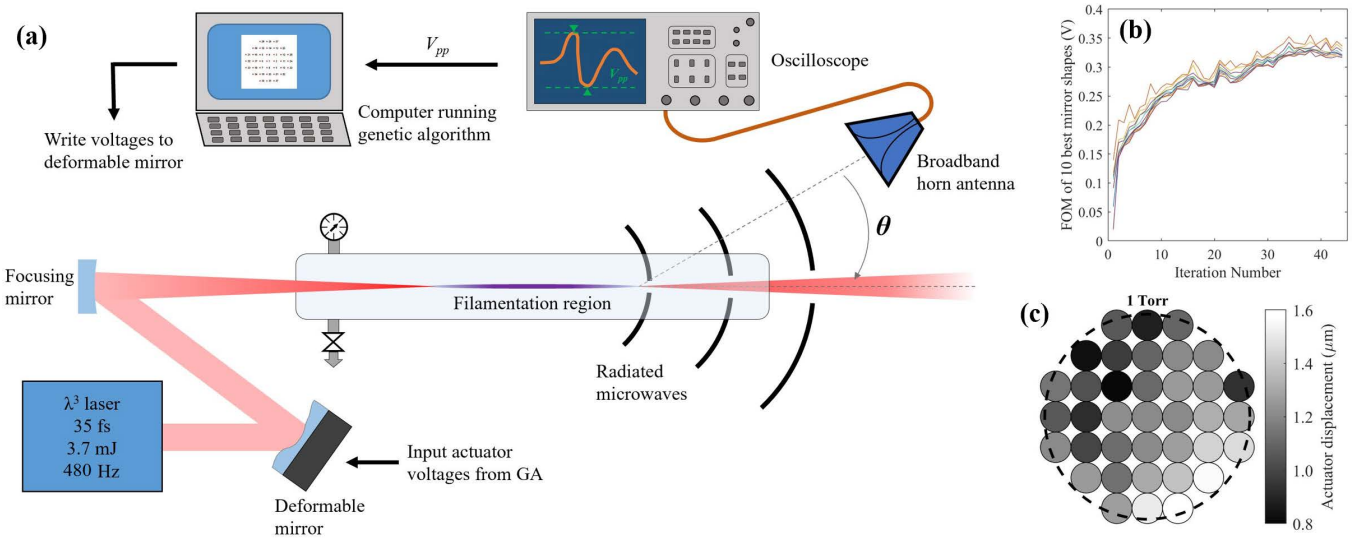

FIG. 1: (a)The experimental setup for the microwave optimization using a deformable mirror. The pulse wavefront is modified by the deformable mirror before reflecting from the surface of the focusing mirror. The microwaves generated by the laser plasma are collected by a 2-18 GHz horn antenna and the waveforms are recorded using a 13 GHz oscilloscope. (b) A typical plot of the FOM (the waveform amplitude V_{pp}) due to the 10 best mirror shapes in each iteration. (c) An example of the actuator configuration and one case of the converged actuator deflections.

The DM used in the experiments is a Xinetics DM37PMNS4, whose actuators are low-hysteresis piezoelectric stacks that are covered by a continuous metallic face sheet. The 37 actuators are arranged in a circular pattern, such as in Fig. 1(c), and the aperture of the mirror is 47 mm. Each actuator has a maximum stroke of 5λ (4 μm at $\lambda = 800$ nm) with resolution better than $\lambda/100$. The actuator deflection is proportional to voltages which are controlled by the GA, and supplied using a multi-channel driver that allows for independent

operation of each actuator. The response of the continuous mirror face to the push and pull of the square-shaped actuators is particular to an individual DM. Further, there is a small amount of mechanical coupling between adjacent actuators. In a traditional closed-loop adaptive optics scheme, it is necessary to determine these responses by quantitatively measuring what are called the influence functions of the actuators. The influence functions are a set of wavefront measurements of a plane wave beam that has been modified by the actuation of each individual DM element.

We do not need to know the influence functions to run our optimization since it is the microwaves that provide feedback to a heuristic search (the GA) as opposed to measuring an aberrated wavefront directly, and instructing the DM to take a shape that cancels the aberrations. The latter is the traditional approach in adaptive optics, as it allows for rapid compensation of the phase usually caused by perturbations from quickly varying atmospheric turbulence, or static and time-dependent aberrations in microscopy and opthalmologic applications. The genetic algorithm on the other hand usually requires several minutes to achieve convergence, but is highly flexible with respect to the quantity being optimized.

In the experiment the pulses propagate through several meters of air before reaching the filamentation region. The evolution of the laser wavefronts will depend on nonlinear contributions over that whole distance in addition to natural diffraction of the pulses. Additionally the pulse propagates through a glass window at the beginning of the glass tube which also affects the propagation. The non-linear phase gained through window contributes to the change in phase front, but as discovered in our previous studies did not effect the emitted RF. A consequence of nonlinear propagation over a long distance and the glass is that a wavefront measurement at a given position cannot be traced backward an arbitrary amount. This concept is called non-reciprocity [40], and it complicates the interpretation of the experiment. The correspondence between the shape of the mirror and the resulting intensity profile is inherently more complex than what occurs in the linear propagation regime. Thus, absent from our measurements are phase profiles recorded in close proximity to the DM or the filamentation region with, for example, a Shack-Hartmann sensor. The pulses would need to be attenuated in order to experimentally measure their wavefront, eliminating its nonlinear contribution. This is the reason that the results described here do not make direct attempts to explain how the shape of the DM corresponds to the optimizations we observe and how the change in beam profile affects the plasma formation. Methods for measuring

the wavefront of a filament are currently under development [41]. Hence we focused on observable plasma properties to study the optimization effect.

B. Genetic Algorithm Implementation

The first step before initializing the GA is to extend all the actuators away from their positions in the unpowered state (30 V are applied to all actuators out of a maximum 100 V). The DM face is reasonably flat when zero voltage is applied to the actuators [42]. Since the driver only supplies positive voltages resulting in actuator displacement outward from the mirror surface, initializing the GA in the vicinity of zero applied voltage might bias its search toward convex mirror shapes.

In order to use a GA, the solution space must be defined in terms of a chosen genetic representation (or basis set). We use the set of 37 independent actuator voltages as the genetic representation of the problem, as this is straightforward to implement. However, other choices of the basis set are possible, for example the coefficients of Zernike polynomials up to a chosen order. If the driver supply for the mirror is capable of K voltage increments between zero and maximum actuator deflection, then our solution space consists of K^{37} possibilities for the mirror shape.

The first GA iteration begins by randomly generating 100 mirror shapes for the initial population. Each mirror shape constitutes a unique individual within the population, and every individuals fitness is scored using a figure of merit (FOM). At the end of each iteration, the 10 individuals with the largest FOMs are advanced to the next iteration and their attributes are crossed over to create the remaining candidates for the next iteration of 100 mirror shapes. If the chosen FOM is valid, then the population evolves toward convergence due to inheritance of optimal actuator positions between iterations. The GA also uses a mutation operator that randomly select actuators and changes their deflection. This accomplishes a broader sampling of the parameter space, with the goal of avoiding convergence to local instead of global extrema. The results presented here use a mutation probability of 20%. This determines both the likelihood of a mutation occurring, and the amplitude of the maximum possible change in the mutated actuators deflection.

The definition of convergence for a GA is usually not rigorous unless the solution is known beforehand. It is common practice to allow the algorithm to run for a set maximum number

of iterations, or to monitor the FOMs as the iterations advance, and declare convergence when the change between iterations becomes small [43]. We use the latter approach to determine convergence. The algorithm stops after the values of the FOMs of the best individuals become relatively steady for several iterations. An example of how the FOM converges is given in Fig. 1(b), which tracks the FOMs of the 10 best individuals from each iteration.

C. Microwave Measurements

The microwave receiver is a broadband horn antenna that has 2-18 GHz bandwidth (American Electronics Laboratories H-1498) connected by a coaxial cable to a 13 GHz oscilloscope (Agilent DSOX91304A). The oscilloscope directly digitizes the voltage waveform that the microwave field induces at the coaxial cable's terminal. The total measurement bandwidth is limited by the oscilloscope on the high frequency side, and the antenna cutoff on the low frequency side, giving an operating frequency range of 2-13 GHz for the experiments. The position of the antenna aperture is a distance of about 1.1 meters from the termination of the plasma. The beam path is elevated about 0.5 meters above the surface of the optical table to provide distance between the plasma and any surfaces that could reflect the radiation. Microwave absorbing foam is placed on the optical breadboard to damp reflections from its surface.

The oscilloscope quickly measures the waveform peak-to-peak voltage, V_{pp}, for feedback to the GA, which we define to constitute optimization of the microwave yield in this experiment. The FOM may explicitly be written as,

$$\text{FOM} = V_{pp} = |v(t)_{max} - v(t)_{min}|, \tag{1}$$

where $v(t)$ is the voltage waveform trace that the oscilloscope records. We use V_{pp} as metric for the microwave yield because for the broadband microwave pulses we are measuring it occurs in the time domain when a large portion of the pulses' frequency components constructively interfere. However, our method is easily adapted to optimize other waveform properties (such as duration, rise time, area under the curve, etc.) or spectral measurements of the microwaves.

After an optimization run is complete the same microwave receiver measures an angular

map of the microwave radiation, in addition to a map resulting from a flat DM (actuator voltages set to zero) at each value of air pressure. The purpose of this is to determine if the wavefronts that give the optimal microwave yield alter the laser pulses in the same way at each pressure, or if the optimization itself exhibits dependence on the air pressure. The angle between the horn and the laser propagation axis is denoted in Fig. 1 as θ, where $\theta = 0^\circ$ is along the laser propagation direction. The microwaves are measured in increments of 5° over an angular range of $\theta = 5^\circ - 55^\circ$. V_{pp} peaks at an angular position of about $\theta \sim 25^\circ - 30^\circ$. Therefore the base test case is to run the GA with the horn at $\theta = 25^\circ$. This is an arbitrary choice, so optimizations at additional angles ($\theta = 5^\circ$ and $\theta = 50^\circ$) are tested when the pressure is 1 Torr, 10 Torr, and 100 Torr along with the base case to determine if the antenna angular position influences the optimization.

III. RESULTS

In order to describe the effect of the GA optimization on the microwave yield, we report measurements of V_{pp}, absolutely calibrated spectra of the electric field, and also the raw waveforms from which the latter two quantities are calculated.

Figure 2 summarizes the outcome of the GA optimizations as a function of air pressure. The GA is able to increase V_{pp} beyond what occurs when the DM is flat, as shown in Fig. 2(a). Although its ability to do so is pressure dependent, with a very small increase at atmospheric pressure, to a doubling of V_{pp} below 10 Torr. Figure 2(b) shows the amount increase as a function of air pressure, given by the ratios of the data points of Fig. 2(a). The cause of the inverse relationship between V_{pp} and pressure in Fig. 2(a) is the reduction in the electron-neutral collision rate. Electron-neutral collisions inhibit the conical electron expansion from the plasma surface. The rate is proportional to pressure, and as it diminishes the current carried by the radial excursion of electrons at the plasma column surface increases, and therefore the longitudinal current that radiates also increases. At some point with decreasing pressure, the magnitude of the longitudinal current has to start dropping again as the density of available charge carriers goes to zero, and we see that roll over starting to take place at 2 Torr in Fig. 2(a) for both cases of a flat and optimized DM.

The pressure dependence of the outcome of the optimization (Fig. 2(b)) could be the result of a few possible circumstances. First, the signal to noise ratio (SNR) of the microwave

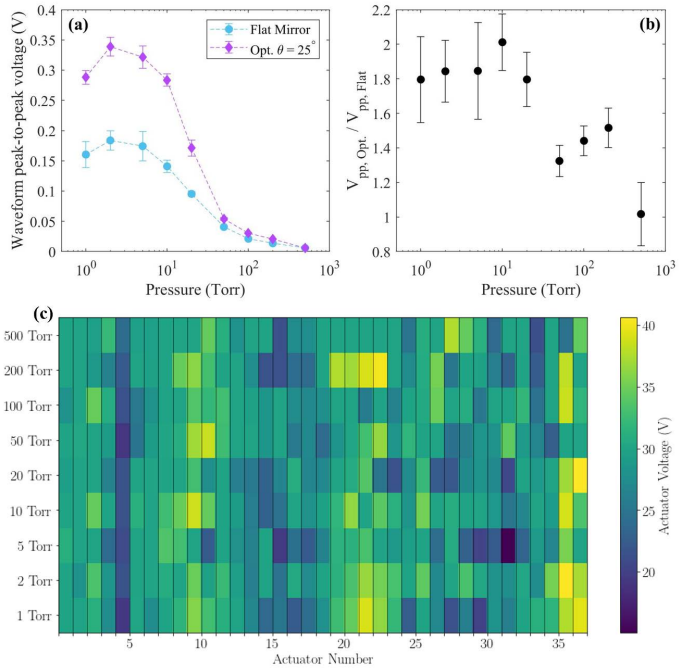

FIG. 2: (a) Waveform peak-to-peak voltage, V_{pp}, versus air pressure when the mirror is flat (blue circles), and when it is optimized (purple diamonds) based on an antenna position of $\theta = 25°$. (b) The increase in the signal amplitude due to the optimization as a function of pressure using the data in panel (a). (c) Heat map of the converged actuator voltages for the optimized mirror shapes for each case of air pressure. Each row of 37 actuator voltages determines the mirror shape for the pressures listed along the ordinate axis. The mirror initial condition is all actuator voltages set to 30 V.

signal near atmospheric pressure is small. The voltage amplitude corresponding to the noise floor of the oscilloscope is approximately 5 mV (including noise internal to the oscilloscope and any continuous sources of environmental microwave background) while for this case V_{pp} is at most about 10 mV. As the GA performs its search at 500 Torr, it is possible that many of the mirror shapes result in microwave radiation that falls below the noise floor, and the value of V_{pp} that gets fed back is simply what the oscilloscope measures for the noise floor. Therefore that we can conclude that the efficacy of the GA depends to some degree on the initial signal level, that is, we cannot expect the GA to turn noise into a signal. Second, it is possible that the pressure dependence of the amount of increase in V_{pp} due to the GA is physical. Intensity clamping inherent to filamentation persists to some

degree even at reduced air pressure with externally focused pulses [44], so the increase in efficacy of the optimization is likely not because the GA is able to greatly enhance the peak intensity at low air pressure any more than it would at higher pressures. Instead the pressure dependence exhibited in Fig. 2(b) may relate to changes in the spatial distribution of plasma that favor radiation at low air pressure. The transition from the possible multi-filament regime at atmospheric pressure to single filament regime at lower pressure may play a role on the microwave emission and the subsequent optimization. We are not able to determine the exact filament placement within the beam profile in this work and how the algorithm changes the pattern. From [24], a similar method demonstrate full control of the filament placement within the beam profile in the single and multi-filament case. Single and multiple filaments can be placed at user-defined areas of the beam in that case. Due to the setup limitation posed by the pressure tube presented in this work, we can not make any statements on how the filament structure affects the microwave emission. We believe that the main reason for minimal optimization at atmospheric pressure is the low signal to noise ratio which poses a challenge for the algorithm to find a good maximum. Additionally the plasma density is believed to be 16 times higher in the focal region [45] where all filaments join to a single so-called superfilament. That region very likely dominates the contribution to the microwave emission. But more research is necessary to investigate the different spatial scenarios and is subject to future work.

The pressure dependence exhibited in Fig. 2(b) leads immediately to the question of what the DM did to the laser pulse wavefronts to produce the increase in microwave yield. While it might seem like wavefront measurements immediately after the DM would directly address the question, we do not believe that it would be possible to immediately link the optimized wavefront shapes to the microwave yield at this time. To our knowledge, there is no existing study that systematically addresses the relationship between general laser beam aberrations and plasma generation in the filamentation regime. Given the issues of non-reciprocal propagation and nonlinearity involved (not just the Kerr effect, but also strong field ionization) such a study would itself be a nontrivial undertaking.

Instead, we can address if there are similarities between the optimized mirror shapes for the various different test cases. To this end, Fig. 2(c) shows the values of the actuator voltages corresponding to the optimized mirror shapes for each value of air pressure. If the GA converged to the same mirror shape for every test case, the vertical bars corresponding

to each actuator in Fig. 2(c) would have uniform color. Qualitatively it is possible that there are some similarities. With few exceptions, the actuator numbering also indicates their physical proximity on the mirror face. It appears as though high and low values of voltage often occur among adjacent actuators. Further, we can see that the mirror shape for the 500 Torr case differs little from the initial condition of 30 V applied to all actuators, which explains why there is no significant change in V_{pp} in that instance.

Ideally we would measure the intensity and beam profile in the focal region for all the different cases. Within a single filament, the intensity is believed to be limited to the clamping intensity of $4.5 \times 10^{13} W cm^2$ [46, 47]. Where as in the focal region and atmospheric pressure a super filament forms with intensities 1.4 times of the initial value [45]. At lower pressures, where filamentatio does not occure, the intesnisty is harder to determine. The glass window at the tube and the vacuum environment exit makes it difficult to image the focal spot since the non-linearity in the glass will affect the beam profile. A more sophisticated experiment is needed to answer the question of how the beam profile and the intensity in the focal region affects the plasma formation in our case. As upper bound we can estimate the peak intensity by using standard gaussian optics assumption, which should be not greater than $1.3 \times 10^{15} W cm^2$. Plasma formation and its defocusing effect reduces the peak intensity very likely to intensities in the order of $10^{14} W cm^2$. Also we were not able to acquire an adequate beam profile to determine hot spots inside the beam at the output of the laser. The lack of being able to adequate analyse the beam profile makes this work hard to compare to our other effort presented in reference [24] .That study focused on the placement and control of the filaments within the initial beam profile which is heavily dependent on the beam profile itself.

In Fig. 3 we show based on the angular pattern of V_{pp} and absolutely calibrated spectral-angular maps of the microwave field that the GA indeed increases the total yield of the radiation, and that the angular position of the antenna when the optimization is performed has little effect on the resulting spatial or spectral characteristics.

Figures 3(a)-(c) compare the angular emission pattern based on V_{pp} when the DM is flat versus the optimized case with an antenna position of $\theta = 25°$. The microwaves are forward directed, and in general the angular maximum in the operating frequency range of the receiver occurs at about $\theta = 25° - 35°$. Figures 3(a)-(c) show that the factor of ~ 2 increase in the microwave yield demonstrated in Fig. 2 is typical across the angular emission

pattern. The optimization therefore achieves an increase in the total conversion efficiency of laser energy to microwave radiation.

One might expect that the optimization would increase the yield along the angular position of the antenna at the expense of radiation emitted in other directions, and therefore that the total radiated power is not changed by the GA. Figure 3 shows that this does not happen. Similar increases in the microwave yield appear to occur regardless of the angular position chosen for the antenna during the optimizations. Figures 3(d)-(f) compare emission patterns measured when the GA has been run with the antenna at $\theta = 5°$, $\theta = 25°$, and $\theta = 50°$. It is possible that the optimizations at $\theta = 25°$ slightly outperform the others, but not beyond the $\sim 15\%$ uncertainty in V_{pp} due to shot-to-shot fluctuations of the laser pulse energy.

While V_{pp} is a convenient metric of the microwave fields in the time domain, it does not rigorously describe their true amplitude and phase because of distortion (attenuation and dispersion) caused by the receiver. We are able to calculate the absolute electric field spectra in free space present at the antenna aperture using calibration data we measured for the receiver, and the Fourier transform of the voltage waveforms that it records. We construct angularly resolved maps of the spectra, and in Figs. 3(g)-(i) show that the indifference of the microwave generation to the angular position of the antenna implied by the V_{pp} measurements in Figs. 3(d)-(f) is a real outcome supported by detailed characteristics of the radiation. A description of the procedure used to calculate the calibrated electric field spectra may be found in the Appendix.

In summary, while we arbitrarily chose to position the antenna at a particular angle of $\theta = 25°$ in order to perform the optimizations, the microwave radiation is ultimately insensitive to this choice. Further, the GA causes an increase in the total microwave yield as opposed to merely increasing the amplitude of radiation emitted in the direction of the antenna aperture.

Figure 4 shows that the effect of the optimizations on the microwave waveforms is to only increase their amplitude. There is no significant difference between the shapes of the waveforms when the mirror is flat versus optimized, that is, the temporal phase of the microwave pulses is apparently unaltered. Figure 4(a) gives examples of waveforms recorded at a fixed pressure of 2 Torr, but at different antenna positions, and Fig. 4(b) shows them at a fixed angle of $\theta = 25°$ but variable pressure. The waveforms have been shifted in

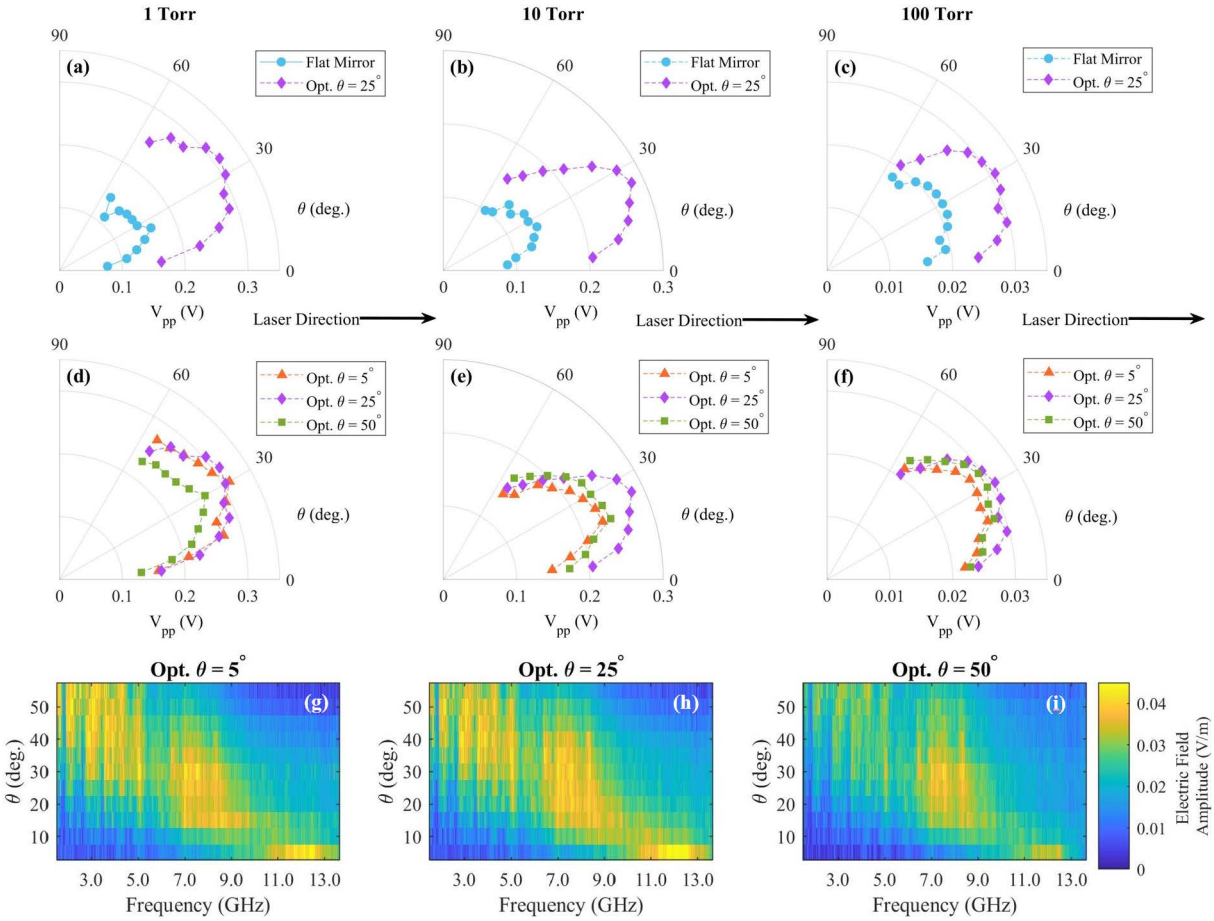

FIG. 3: Angular emission pattern of the microwaves in the time and frequency domains. Panels (a)-(c) compare the patterns found at 1 Torr, 10 Torr, and 100 Torr when the mirror is flat, versus when the microwaves are optimized with the antenna at $\theta = 25°$. Comparison of the same pressure range is shown in panels (d)-(f) for different optimization cases: when the antenna is at $\theta = 5°$ (orange triangles), $\theta = 25°$ (purple diamonds), and $\theta = 50°$ (green squares). The arrows in between the first and second row of panels indicate the laser propagation direction. (g)-(i) Absolutely calibrated spectral-angular maps of the microwave electric field corresponding to the cases of antenna position during optimizations performed at 1 Torr, i.e. the three cases of Opt. θ shown in panel (d).

time to align their features so that the shape comparison is clear. While the increase in waveform amplitude was already indicated in Figs. 2 and 3 by V_{pp}, the fact that the DM optimization causes no concomitant modification to the temporal phase over the ranges of pressure and angular position is interesting. This means that the wavefront manipulation

results in a greater current flowing in the plasma, or more efficient conversion of the current to radiation, but that the time evolution (subject to the frequency limits of our receiver) of the source currents is insensitive to the wavefront shape.

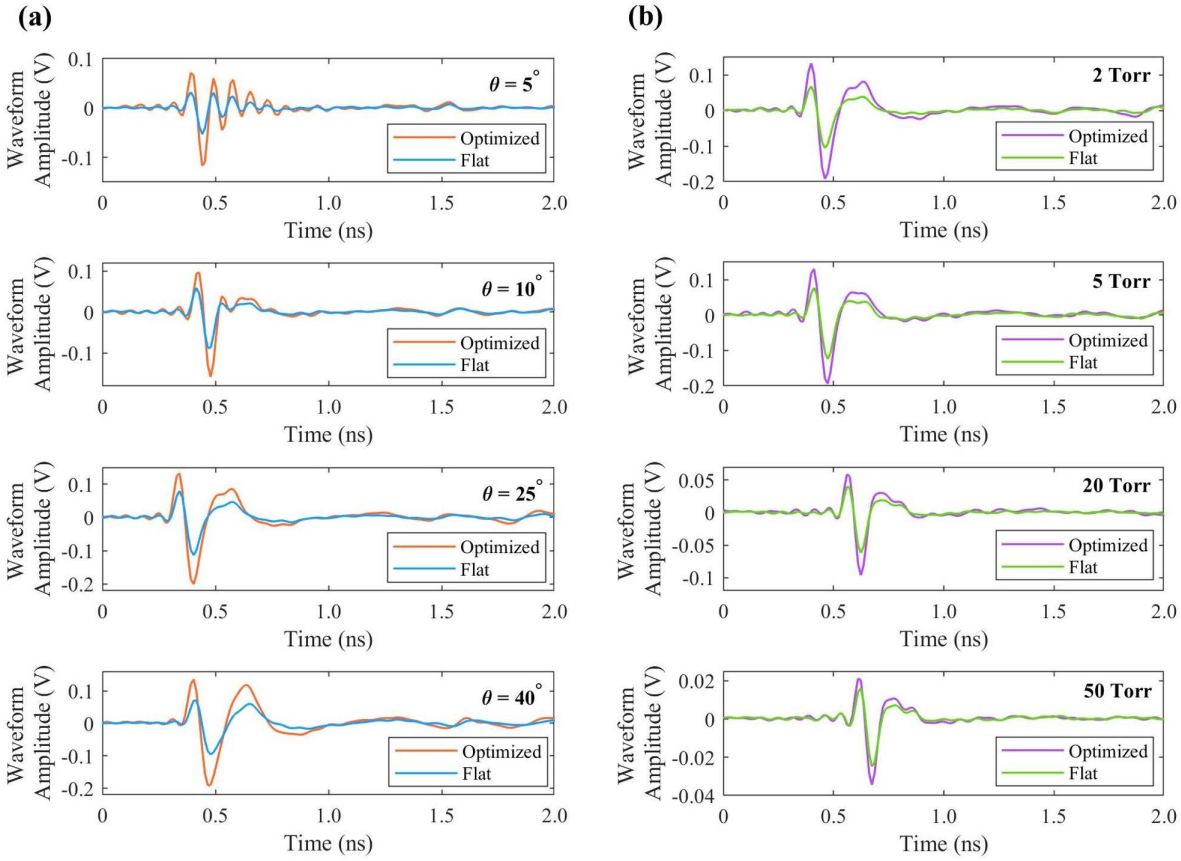

FIG. 4: (a) The first column of waveforms compares the optimized and flat cases as a function of emission angle at a fixed pressure of 2 Torr. (b) The second column also compares the optimized and flat cases, but as a function of air pressure. The waveforms in (b) are recorded at a fixed angular position of $\theta = 25°$.

Some notable characteristics present in the waveforms of Fig. 4 have been documented before. We briefly acknowledge them here for the sake of experimental reproducibility. The tendency of high frequency components of the field to radiate near the laser axis ($\theta \to 0°$) and the relative increase in the amplitude of low frequency components with decreasing air pressure were noted in Refs. [33, 37, 38]. In this experiment, the time variations of the waveform become slower in Fig. 4(a) as θ increases from 5° to 40°. In Fig. 4(b), as the pressure drops from 50 Torr to 2 Torr, the duration of the main cycle of the pulse increases

from about 400 ps to about 600 ps, and additional low-frequency field cycles appear after $t = 1.0$ ns. The temporal shape of the signal correlates the RF rise time and fall times to the plasma temperature. Hydrodynamic modeling would allow for the determination of such temperature. However dispersion in the RF and microwave equipment, such as the cable and the antenna, is not well known in our experiment and no easy scaling law can be applied to correlate the measured signal to the detection system rise and fall times.

The temporal, spectral, and spatial data we present for the microwaves as a function of air pressure shows that the GA is able to optimize the laser wavefront to increase the total power of the radiation. It is interesting that the efficacy of the optimization depends on air pressure, and that the increase in conversion efficiency of the microwaves occurs without modifying aspects of the microwaves other than their amplitude.

IV. DISCUSSION

We have shown that the GA optimization of the microwave generation is possible. We increase the microwave yield by 2x in the best case. This is vastly different than the 6x increase of THz yield in a experiment using two color filamentation. We contribute the difference to the different in mechanisms. Broadband THz spectra generated by the two color plasma generation, as demonstrated in reference [28] have multiple origins depending on their frequency range. In the low frequency region (1 THz to 5 THz), the free-electron photocurrent is the major contribution to THz radiation. As the frequency increases beyond 5 THz, the Kerr nonlinear response of the neutral molecules, which is related to four wave mixing, dominates. In those two color experiment, it is believed that adaptive control of the wavefront improves and manipulates the phase of both the fundamental and the second harmonic fields, leading to the significant enhancement in the THz radiation. Where as in our experiment we only use a single color process for RF and microwave. We believe surface waves propagate along the filament plasma and detach at its end which results in an RF pulse emitted [28, 33]. The process is dominated by the electron-neutral collisions and the plasma expansion and we expected only a small increase in microwave energy by manipulate the wavefront of the laser. We achieve a much larger increase by simply reducing the pressure of the propagating gas which reduces the electron-neutral collision frequency.

The nature of the optimization can be understood by employing a similarity measure

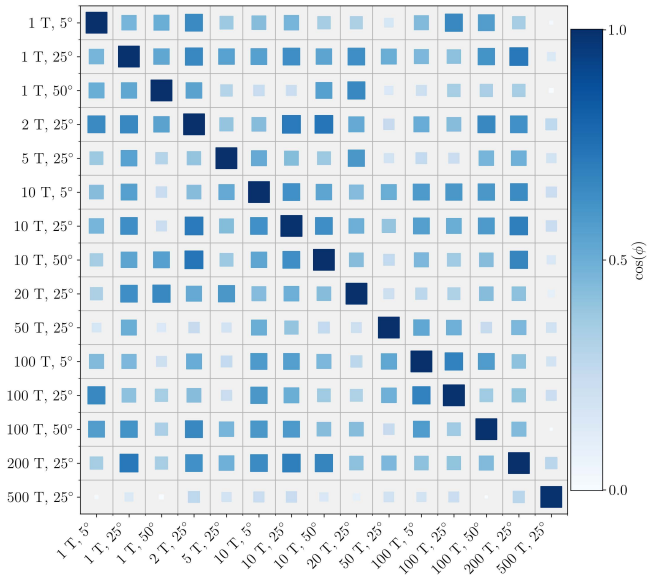

FIG. 5: Correlation map of the cosine similarity between the converged actuator positions of each of the test cases. We have abbreviated the units Torr as 'T'. The color scale and box size indicate the value of $\cos(\phi)$, where larger and darker boxes indicate a greater degree of similarity. The diagonal represents the degenerate instances where each vector of actuator voltages is compared to itself.

among the mirror shapes for the test cases. In Fig. 5 we calculate the cosine similarity based on the actuator voltages for all the cases of air pressure and antenna position during optimization shown and present them in the form of a correlation map. Cosine similarity is a common tool used in applications of machine learning such as natural language processing and computer vision to assess differences between objects with many degrees of freedom, for example pixels in a digital image, and reduce the degree of similarity to a single number. If we consider the 37 actuator voltages to each be components of a vector, then the cosine of the angle between two sets of actuator voltages ($\mathbf{u}$ and $\mathbf{v}$) is given by

$$\cos\phi = \frac{\sum_{i=1}^{37} u_i v_i}{\sqrt{\sum_{i=1}^{37} u_i^2}\sqrt{\sum_{i=1}^{37} v_i^2}}, \tag{2}$$

where $\cos\phi = 1$ indicates the maximum similarity, and $\cos\phi = 0$ indicates complete dissimilarity (the vectors are orthogonal). To compute $\cos\phi$, we first subtract 30 V from all

the values of actuator voltage, which re-centers the vectors about a meaningful origin, since the initial condition of the GA is to drive all actuators at 30 V. The result is a significant amount of variation in $\cos\phi$ that does not appear to have trends with air pressure, or exhibit clustering among cases of constant pressure but a difference in the position of the antenna during the optimization. If there were clear trends of $\cos\phi$ with pressure, we would expect to see larger values near the diagonal, and small values in the off-diagonal portions of the correlation map. For the 500 Torr case, the lack of actuator modulation shown in Fig. 2(c) means that there is negligible similarity with the other test cases. One implicit assumption in using $\cos\phi$ in this manner is that each degree of freedom is completely independent of the others. Given the small amount of mechanical coupling between adjacent actuators we know that such independence is a low-order approximation. Therefore, $\cos\phi$ in this instance should be regarded only as a semi-quantitative similarity measure of the optimized mirror shapes.

However what we can say by considering Fig. 2(c) along with Fig. 5, given that outcome of the GA optimization is highly repeatable (a similar increase in V_{pp} is achieved for many different test cases) is that the shape of the solution space for the particular optimization we have sought appears to be relatively flat in the vicinity of the extremum (or extrema) to which the GA converges. Put another way, it is not necessary to always find the precise mirror shape out of all the possibilities in order to achieve the results we have measured. A similar observation was made in Ref. [28] for the optimization of THz generation from single and two-color laser pulses, where the THz field strength was found to be reproducible even if the exact mirror shape differed among test cases. The relative insensitivity of the microwave and THz enhancement to the exact mirror shape may be caused by the external focusing applied to the pulses ($f/40$ here, and $f/15$ in Ref. [28]) because the focusing optics impart a significant amount of focusing curvature to the wavefronts, upon which the DM manipulation could be merely a small perturbation.

The plasma generation in the filament wake appears to be similarly repeatable in spite of the differences in the optimized mirror shapes. Fig. 6 shows the plasma fluorescence observed with the ICCD camera at each pressure, and compares the plasma produced by each flat and optimized case. In the images, the laser propagates from right to left. The optimized mirror shapes generally produce longer and brighter regions of plasma fluorescence which correlates with an increase in microwave signal. A similar effect is observed by just reducing

FIG. 6: Comparison of images of the filament plasma fluorescence when the mirror is flat (left column) versus optimized with the antenna at $\theta = 25°$ (right column). The direction of laser propagation is right to left. A length scale is given in at the top of the left column. The typical length of the plasma fluorescence with the DM flattened is about 4 cm.

the pressure where the fluorescence is increase at lower pressure. The plasma also appears to be wider in the direction transverse to the laser propagation at the lowest values of air pressure. Interestingly, this is in contrast to the results of the THz optimization for which the plasma was also elongated, but whose fluorescence was significantly dimmer than when the DM was flat [28]. The increase in the volume of fluorescing plasma indicates that the total energy of the electron population is greater (either because there is more ionization, a greater proportion of electrons have sufficient energy for impact excitation of heavy species, or both) which points to an increase in the laser intensity through the focal region due to the optimizations. We note for the case of 500 Torr, where Fig. 2(b) shows no improvement by the GA, and the actuator voltages in Fig. 2(c) indicate that the mirror shape does not change significantly, the plasma fluorescence also shows little difference for the flat versus optimized cases. The optimized mirror shapes appear to perturb the focus imposed by the concave mirror randomly as a function of pressure. Along with the small-scale fluctuations in the shape of the plasma, these factors likely cause the small variations in microwave angular

distribution observed among the optimization cases in Fig. 3. The increase in brightness and volume of the plasma fluorescence are the repeatable characteristics among the optimized test cases. Investigating the plasma radius and the plasma length individually is difficult since they are inherently coupled. One cannot simply change the focusing conditions a change in only one parameter. Particular the dependence on the plasma radius and the f-number is expected to by non-linear and cannot easily scaled. We have already demonstrated that length does have an effect on the microwave emitted [48]. More work is required to have a definitive answer on how the radius effects the microwave emission.

Estimates of the plasma size extracted from the images in Fig. 6 are given in Fig. 7. It is not accurate to say that the size of the plasma is the same as the size of the region that produces fluorescence [49]. However, we make the assumption that the size of the fluorescence correlates to the true size of the plasma. Figure 7 also shows intensity profiles of the fluorescence calculated by integrating in the longitudinal and transverse dimensions of the images. Each profile in Figs. 7(a)-(d) is an average of 10 profiles from repetitive images of the plasma. The camera was mounted at a slight angle to the direction normal to propagation. This rotation is removed before integrating the images so that the longer plasmas do not appear to be fictitiously wider.

In Fig. 7(a) when the mirror is flat, the plasma appears to have two longitudinally separated regions of fluorescence, with the brighter of the two toward the termination of the filament region. The two fluorescing regions might indicate the presence of astigmatism in the focus. The effect of the mirror optimization as seen in Fig. 7(b) is either to eliminate the separation between the high brightness regions in the plasma, or to shift the brighter one closer to the beginning of the filament region. The examples shown at 2 Torr, 20 Torr, and 200 Torr are representative of the length profiles at all the cases shown in Fig. 6. The implication of the shape change of the fluorescence profile, and the increase in brightness may be that the DM removes aberrations from the wavefronts, for example opposing the astigmatism that could exist when the DM is flat. However careful characterization of the laser pulses uprange and downrange of the DM both with and without the optimized mirror shape, along with propagation simulations, would be needed to confirm such an effect.

The increase in magnitude of the fluorescence profiles between Fig. 7(c) and Fig. 7(d) reflects both the brightness and length of the plasmas due to the integration in the longitudinal dimension. Comparing the peak values of the profiles shows about a factor of 2

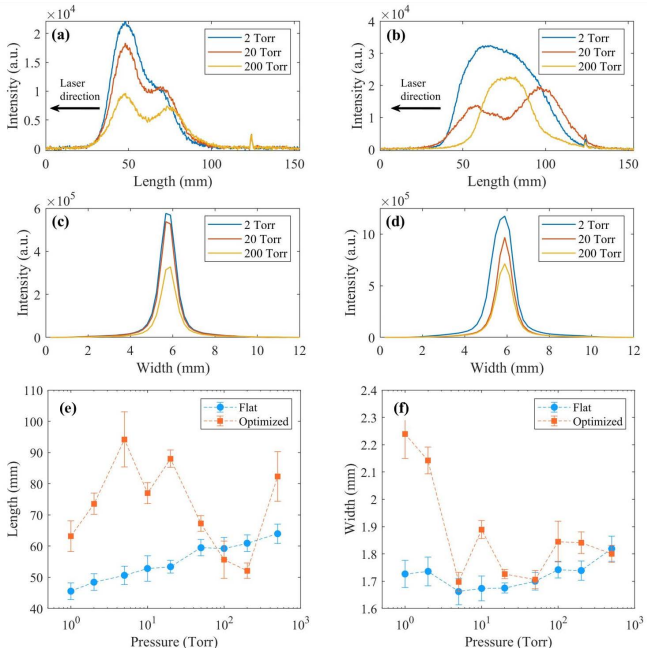

FIG. 7: Intensity profile of the plasma fluorescence in the longitudinal direction found by integrating in the transverse dimension when the DM is (a) flat versus (b) optimized. The arrows indicate the direction of laser propagation. The transverse intensity profiles for the (c) flat and (d) optimized mirror shapes are calculated by integrating along the longitudinal dimension. (e) Length and (f) width of the plasma fluorescence as a function of air pressure, comparing the flat (blue circles) to optimized (orange squares) cases.

increase between the flat and optimized cases, which agrees with the increase measured for V_{pp}. Other experiments performed in the same frequency range, and a similar focal geometry (but no DM) have shown that the field strength of the microwaves has a complicated dependence on the peak intensity of the input pulses, since it determines the maximum of the electron energy distribution in addition to the spatial dimensions of the plasma [48]. In particular, the plasma length influences the microwave field strength because the field constructively interferes along the plasma as the laser pulse propagates, so longer plasmas result in greater coherent buildup of the microwaves.

Figures 7(e)-(f) shows the length and width of the fluorescence as a function of pressure, based on the $1/e^2$ threshold of the longitudinal and transverse profiles, respectively. The plasma becomes shorter at low pressure if the DM is flat. The nonlinear response of the air decreases with pressure, and the contribution of self-focusing to the pulse propagation

diminishes causing the plasma generation to take place closer to the Rayleigh range of the concave mirror and filamentation is not occurring at pressures below 76 Torr. With the DM flat, the width given in Fig. 7(f) appears to be roughly constant with air pressure. Figures 7(e) and (f) show that the optimization generally increases the length and width of the plasma.

It is important to note some systematic biases in the profiles of the plasma width in Figs. 7(c)-(d) which affect the numerical values reported in Fig. 7(f). The first is that the images are composed to fit the whole plasma at once, so the resolution in the transverse direction is low. The second is that the curvature of the gas cell (quartz tube) is in the direction of the transverse dimension which gives the plasma images a small cylindrical distortion, whose effect is likely a slight magnification of the width. However, the relative differences in the width and brightness of the plasma are real, and the absolute numerical values of the width of the plasma fluorescence are not consequential to our conclusions. As mentioned above the decoupling of radius and and length is a non-trivial task. We are currently working on experiments that address the contribution of the radius to further the understanding.

An increase in the laser intensity implied by the plasma fluorescence may also be inferred from apparent changes in the beam mode due to the GA optimization. Figure 8 shows examples of the beam mode of the laser before and after optimizing the microwave yield. The object plane is located at the termination of the laser plasma when the when the DM is flat. The mode content of the beam with the flat DM in Fig. 8(a) includes significant aberrations, as the image has a starburst shape with bright tails extending far from the center of the beam. These features are not present in Fig. 8(b). The optimization of the microwave yield causes the beam to have a more circular shape. The optimized intensity increase could result in a substantial increase in plasma density. The highly non-linear nature of the multi-photon ionization ($\propto I^n$, where n is the number of photons) could result in a 2x increase. However, the exact link of microwave emission to the density is not quite established and subject to ongoing research. The same is true for electron temperature and how it effects the amplitude of wave on the surface of the plasma. We can for certain say that the electron-neutral collision frequency dominates as demonstrated by reducing the gas pressure [33, 37].

The images demonstrate that the microwave yield is connected to the transverse shape

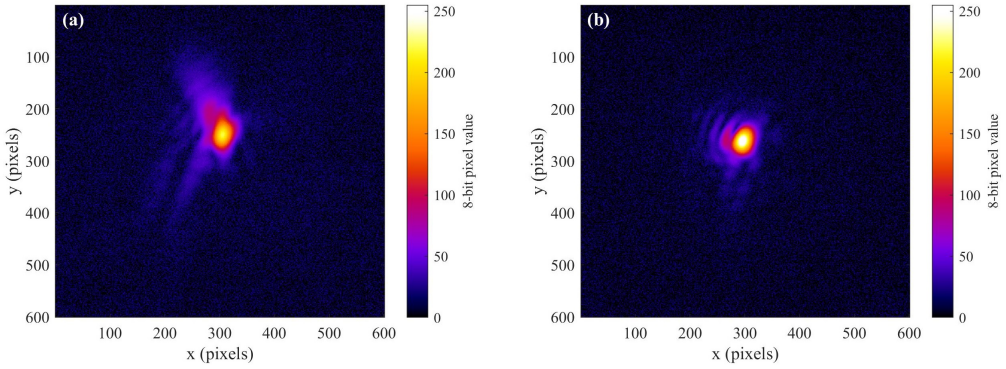

FIG. 8: Images of the beam mode at the filament termination when the air pressure is 2 Torr (a) before optimization and (b) after optimization. For this particular case, images of the plasma fluorescence in Fig. 6 indicate that the end of the plasma does not shift longitudinal position significantly due to the optimization.

of the laser pulses, but the detailed nature of the dependence must be left to future investigations. This is because the far field beam profiles in Fig. 8 may not simply be magnified images of the true intensity profile that exists at the termination of the laser plasma. The laser energy deposition in the filament plasma is at most 10% [6, 50] so sufficient power remains in the pulse after ionizing the air for it to propagate nonlinearly in the air outside the gas cell, and especially in its thin exit window. Unfortunately, the general shape of the beam is the only usable information, and only in the most topical sense. The issue could be resolved in by taking a weak surface reflection from a glass wedge placed near the termination of the filamentation region. However, this cannot be practically implemented inside the gas cell. A re-designed gas cell that incorporates a wedge and a thin vacuum window to transmit reflections that reliably capture the intensity profile will be used in future experiments.

V. CONCLUSION

The experiment demonstrates that wavefront manipulations controlled by a GA are a versatile method for optimizing microwave radiation from filament plasmas. It would have been difficult to manually identify and construct wavefronts that increase the microwave yield, and it was not clear beforehand any increase in the radiation was possible via wavefront

manipulation. Although the cost of the GA's versatility is the ambiguous mapping between a particular wavefront configuration and the results we have observed.

The temporal, spectral, and spatial characteristics of the waveforms demonstrate an increase the total microwave yield, but the amount of increase itself is pressure dependent. While a factor of two is achieved at the lowest pressures we tried, a smaller increase is seen at higher pressures, and no improvement near atmospheric pressure. The pressure dependence of the optimization's efficacy either results from a tendency of the GA to perform better when the initial signal levels are larger, or is related to the spatial distribution of plasma resulting from the optimizations that allows for greater radiation at low air pressure.

Pinpointing the causes of the increase is difficult in part because of the nonlinearity of the laser propagation and plasma generation, but also because we have observed that it is possible to achieve a repeatable enhancement of the microwaves with mirror shapes that may have some similarities, but clearly are not the same.

Images of the plasma fluorescence and far field beam profile before and after the optimization provide a partial explanation. The optimized wavefronts increase the length and the brightness of the plasma, and alter the beam mode leaving the filamentation region. The increase in the plasma fluorescence is highly repeatable in spite of the differences in the optimized mirror shapes. The optimization also appears to make the beam profile more circular than if the mirror is flattened. These imply an increase in the pulse intensity through the filamentation region. This increase in intensity must occur slightly off axis, since the peak intensity is still limited by intensity clamping. This agrees with the observed increase in the volume of fluorescing plasma, and the pressure dependence of the GA's efficacy.

This experiment suggests several possibilities for additional experiments and simulations. In particular, the ambiguities that arise in this study (different mirror shapes cause the same increase in microwave generation) call for systematic exploration of the effects of general beam aberrations on the propagation of the filaments and the plasmas they generate.

Also, a similar experiment to this one could be performed to see if optimization of other characteristics of the microwave field is possible. For example, given the invariance of the temporal phase with the optimization in this experiment, is it possible to force changes in the waveform shape by maximizing the microwave rise time, or selecting a subrange of the receiver bandwidth to increase, while minimizing the other spectral content? The GA is a convenient tool for prototyping experiments of this nature, even if an immediate physical

connection between input and outcome is elusive.

Finally, our experiment could eventually find a practical application in high intensity laser science. The increase in intensity resulting from optimizing the microwave yield may provide a method for automatically finding the best laser focus. This would require further study than what we have presented, including careful measurement of the laser focal spot in vacuum, as well as wavefront characterizations. If a connection between the microwave yield and the optimal focal intensity were established, it would provide a relatively straightforward way to correct the final focusing of intense ultrashort laser pulses without manual realignment.

VI. FUNDING

This material is based upon work supported by the Air Force Office of Scientific Research under award numbers FA9550-16RDCOR325, FA9550-19RDCOR027, FA9550-16-1-0121, and the Department of Energy/High Energy Physics under grant number DE-SC0016804. A.E. acknowledges support from the U.S. Naval Research Laboratory through the Jerome and Isabella Karle Postdoctoral Fellowship.

VII. DISCLOSURES

The authors declare no conflicts of interest.

VIII. DATA AVAILABILITY STATEMENT

Data underlying the results presented in this paper are not publicly available at this time but may be obtained from the corresponding author upon reasonable request.

Appendix: Electric Field Calibrations

The calibration procedure for the microwave spectra has two parts: measurement of the antenna gain, and measurement of the frequency-dependent loss through the rest of the receiver (the coaxial cable and the oscilloscope). The antenna gain is measured using the two-antenna technique, and the loss is measured by connecting the coaxial cable to a

broadband reference noise source. This allows us to present spectra in terms of the microwave electric field in free space incident on the antenna aperture by using the definition of the antenna factor.

$$E(f) = \frac{V(f)}{X(f)}\sqrt{\frac{4\pi\eta_0}{\lambda^2 Z_L G(f)}}. \tag{A1}$$

The antenna factor is the ratio of the electric field $E(f)$ to the voltage induced on the antenna's terminal $E(f)/V_{term}(f)$, and is given in Eq. A1 by the square root term, where $\eta_0 = 377\ \Omega$ is the impedance of free space, λ is the microwave wavelength, Z_L is the antenna output impedance (here $Z_L = 50\ \Omega$) and $G(f)$ is its frequency-dependent gain. The voltage present across the antenna terminal is given by $V_{term}(f) = V(f)/X(f)$, where $V(f)$ is the real part of the Fourier transform of the voltage waveform $v(t)$, and $X(f)$ is the frequency-dependent loss measured for the coaxial cable and oscilloscope.

IX. REFERENCES

[1] A. Braun, G. Korn, X. Liu, D. Du, J. Squier, and G. Mourou, Optics Letters **20**, 73 (1995), URL http://ol.osa.org/abstract.cfm?URI=ol-20-1-73.

[2] A. Couairon and A. Mysyrowicz, Physics Reports **441**, 47 (2007), ISSN 0370-1573, URL http://www.sciencedirect.com/science/article/pii/S037015730700021X.

[3] D. Mongin, E. Schubert, N. Berti, J. Kasparian, and J.-P. Wolf, Phys. Rev. Lett. **118**, 133902 (2017), URL https://link.aps.org/doi/10.1103/PhysRevLett.118.133902.

[4] S. Tzortzakis, L. Bergé, A. Couairon, M. Franco, B. Prade, and A. Mysyrowicz, Phys. Rev. Lett. **86**, 5470 (2001), URL https://link.aps.org/doi/10.1103/PhysRevLett.86.5470.

[5] S. A. Hosseini, Q. Luo, B. Ferland, W. Liu, S. L. Chin, O. G. Kosareva, N. A. Panov, N. Aközbek, and V. P. Kandidov, Physical Review A **70**, 033802 (2004), URL https://link.aps.org/doi/10.1103/PhysRevA.70.033802.

[6] D. Pushkarev, E. Mitina, D. Shipilo, N. Panov, D. Uryupina, A. Ushakov, R. Volkov, A. Karabutov, I. Babushkin, A. Demircan, et al., New Journal of Physics **21**, 033027 (2019), URL https://doi.org/10.1088%2F1367-2630%2Fab043f.

[7] F. Courvoisier, V. Boutou, J. Kasparian, E. Salmon, G. Méjean, J. Yu, and J.-P. Wolf, Appl. Phys. Lett. **83**, 213 (2003), URL https://doi.org/10.1063/1.1592615.

[8] A. M. Heins and C. Guo, Appl. Phys. B **113**, 317 (2013), URL https://doi.org/10.1007/s00340-013-5483-5.

[9] S. Suntsov, D. Abdollahpour, D. G. Papazoglou, and S. Tzortzakis, Appl. Phys. Lett. **94**, 251104 (2009), URL https://doi.org/10.1063/1.3157908.

[10] V. Kandidov, N. Akozbek, M. Scalora, O. Kosareva, A. Nyakk, Q. Luo, S. Hosseini, and S. Chin, Applied Physics B **80**, 267 (2005), ISSN 1432-0649, URL https://doi.org/10.1007/s00340-004-1677-1.

[11] D. E. Shipilo, N. A. Panov, E. S. Sunchugasheva, D. V. Mokrousova, V. A. Andreeva, O. G. Kosareva, L. V. Seleznev, A. B. Savel'ev, A. A. Ionin, and S. L. Chin, Laser Physics Letters **13**, 116005 (2016), URL https://doi.org/10.1088%2F1612-2011%2F13%2F11%2F116005.

[12] P. Rohwetter, M. Queißer, K. Stelmaszczyk, M. Fechner, and L. Wöste, Physical Review A **77**, 013812 (2008), URL https://link.aps.org/doi/10.1103/PhysRevA.77.013812.

[13] P. Polynkin, M. Kolesik, J. V. Moloney, G. A. Siviloglou, and D. N. Christodoulides, Science **324**, 229 (2009), ISSN 0036-8075, URL https://science.sciencemag.org/content/324/5924/229.

[14] G. Fibich, S. Eisenmann, B. Ilan, and A. Zigler, Optics Letters **29**, 1772 (2004), URL http://ol.osa.org/abstract.cfm?URI=ol-29-15-1772.

[15] N. Barbieri, Z. Hosseinimakarem, K. Lim, M. Durand, M. Baudelet, E. Johnson, and M. Richardson, Appl. Phys. Lett. **104**, 261109 (2014), URL https://doi.org/10.1063/1.4886960.

[16] P. Béjot, G. Karras, F. Billard, J. Doussot, E. Hertz, B. Lavorel, and O. Faucher, Phys. Rev. A **92**, 053417 (2015), URL https://link.aps.org/doi/10.1103/PhysRevA.92.053417.

[17] M. Scheller, M. S. Mills, M.-A. Miri, W. Cheng, J. V. Moloney, M. Kolesik, P. Polynkin, and D. N. Cristodoulides, Nat. Photon. **8**, 297 (2014), URL https://doi.org/10.1038/nphoton.2014.47.

[18] P. Sprangle, J. R. Peñano, and B. Hafizi, Phys. Rev. E **66**, 046418 (2002), URL https://link.aps.org/doi/10.1103/PhysRevE.66.046418.

[19] M. P. Ross, B. M. L. Pascoguin, A. Hening, and B. Lynn, J. of Appl. Phys. **128**, 154903 (2020), URL https://doi.org/10.1063/5.0023222.

[20] J.-F. Daigle, Y. Kamali, J. Bernhardt, W. Liu, C. Marceau, A. Azarm, and S. Chin, Opt. Comm. **281**, 3327 (2008), ISSN 0030-4018, URL https://www.sciencedirect.com/science/article/pii/S0030401808001879.

[21] A. A. Ionin, N. G. Iroshnikov, O. G. Kosareva, A. V. Larichev, D. V. Mokrousova, N. A. Panov, L. V. Seleznev, D. V. Sinitsyn, and E. S. Sunchugasheva, Journal of the Optical Society of America B **30**, 2257 (2013), URL http://josab.osa.org/abstract.cfm?URI=josab-30-8-2257.

[22] D. V. Apeksimov, Y. E. Geints, A. A. Zemlyanov, A. M. Kabanov, V. K. Oshlakov, A. V. Petrov, and G. G. Matvienko, Appl. Opt. **57**, 9760 (2018), URL http://ao.osa.org/abstract.cfm?URI=ao-57-33-9760.

[23] T. Pfeifer, L. Gallmann, M. J. Abel, D. M. Neumark, and S. R. Leone, Opt. Lett. **31**, 2326 (2006), URL http://ol.osa.org/abstract.cfm?URI=ol-31-15-2326.

[24] A. C. Englesbe, Z.-H. He, J. A. Nees, A. G. R. Thomas, A. Schmitt-Sody, and K. Krushelnick, Opt. Express **24**, 6071 (2016), URL http://www.opticsexpress.org/abstract.cfm?URI=oe-24-6-6071.

[25] L. Finney, J. Lin, P. Skrodzki, M. Burger, J. Nees, K. Krushelnick, and I. Jovanovic, Opt. Commun. **490**, 126902 (2021), ISSN 0030-4018, URL https://www.sciencedirect.com/science/article/pii/S0030401821001528.

[26] R. Ackermann, E. Salmon, N. Lascoux, J. Kasparian, P. Rohwetter, K. Stelmaszczyk, S. Li, A. Lindinger, L. Wöste, P. Béjot, et al., Applied Physics Letters **89**, 171117 (2006).

[27] J.-F. Daigle, Y. Kamali, M. Châteauneuf, G. Tremblay, F. Théberge, J. Dubois, G. Roy, and S. L. Chin, Applied Physics B **97**, 701 (2009), ISSN 1432-0649, URL https://doi.org/10.1007/s00340-009-3713-7.

[28] J. Hah, W. Jiang, Z.-H. He, J. A. Nees, B. Hou, A. G. R. Thomas, and K. Krushelnick, Optics Express **25**, 17271 (2017), URL http://www.opticsexpress.org/abstract.cfm?URI=oe-25-15-17271.

[29] J. Lin, Y. Ma, R. Schwartz, D. Woodbury, J. A. Nees, M. Mathis, A. G. R. Thomas, K. Krushelnick, and H. Milchberg, Opt. Express **27**, 10912 (2019), URL http://www.opticsexpress.org/abstract.cfm?URI=oe-27-8-10912.

[30] Z.-H. He, B. Hou, G. Gao, V. Lebailly, J. A. Nees, R. Clarke, K. Krushelnick, and A. G. R. Thomas, Physics of Plasmas **22**, 056704 (2015).

[31] S. J. D. Dann, C. D. Baird, N. Bourgeois, O. Chekhlov, S. Eardley, C. D. Gregory, J.-N. Gruse, J. Hah, D. Hazra, S. J. Hawkes, et al., Phys. Rev. Accel. Beams **22**, 041303 (2019), URL https://link.aps.org/doi/10.1103/PhysRevAccelBeams.22.041303.

[32] J. H. Holland, *Adaptation in natural and artificial systems* (University of Michigan Press, 1975).

[33] T. Garrett, J. Elle, M. White, R. Reid, A. Englesbe, R. Phillips, P. Mardahl, A. Schmitt-Sody, E. Thornton, J. Wymer, et al., *Generation of RF by atmospheric filaments*, https://arxiv.org/abs/2102.12657 (2021), 2102.12657.

[34] A. Englesbe, J. Elle, R. Schwartz, T. Garrett, D. Woodbury, D. Jang, K.-Y. Kim, H. Milchberg, R. Reid, A. Lucero, et al., Phys. Rev. A (Submitted) (2021).

[35] K. Y. Kim, J. H. Glownia, A. J. Taylor, and G. Rodriguez, Optics Express **15**, 4577 (2007), URL http://www.opticsexpress.org/abstract.cfm?URI=oe-15-8-4577.

[36] H. Roskos, M. Thomson, M. Kreß, and T. Löffler, Laser & Photonics Reviews **1**, 349 (2007), URL https://onlinelibrary.wiley.com/doi/abs/10.1002/lpor.200710025.

[37] A. Englesbe, J. Elle, R. Reid, A. Lucero, H. Pohle, M. Domonkos, S. Kalmykov, K. Krushelnick, and A. Schmitt-Sody, Optics Letters **43**, 4953 (2018), URL http://ol.osa.org/abstract.cfm?URI=ol-43-20-4953.

[38] A. V. Mitrofanov, D. A. Sidorov-Biryukov, M. M. Nazarov, A. A. Voronin, M. V. Rozhko, A. B. Fedotov, and A. M. Zheltikov, Opt. Lett. **46**, 1081 (2021), URL http://ol.osa.org/abstract.cfm?URI=ol-46-5-1081.

[39] B. Hou, J. Easter, A. Mordovanakis, K. Krushelnick, and J. A. Nees, Optics Express **16**, 17695 (2008), URL http://www.opticsexpress.org/abstract.cfm?URI=oe-16-22-17695.

[40] J. P. Palastro, J. Peñano, W. Nelson, G. DiComo, M. Helle, L. A. Johnson, and B. Hafizi, Optics Express **24**, 18817 (2016), URL http://www.opticsexpress.org/abstract.cfm?URI=oe-24-17-18817.

[41] D. Thul, M. Richardson, and S. Rostami Fairchild, Sci. Rep. **10**, 8920 (2020), URL https://doi.org/10.1038/s41598-020-65431-0.

[42] Z.-H. He, Ph.D. thesis, University of Michigan (2014).

[43] D. Greenhalgh and S. Marshall, SIAM Journal on Computing **30**, 269 (2000), ISSN 0097-5397, URL https://doi.org/10.1137/S009753979732565X.

[44] A. Couairon, M. Franco, G. Méchain, T. Olivier, B. Prade, and A. Mysyrowicz, Opt. Comm.

259, 265 (2006).

[45] G. Point, Y. Brelet, A. Houard, V. Jukna, C. Milián, J. Carbonnel, Y. Liu, A. Couairon, and A. Mysyrowicz, Phys. Rev. Lett. **112**, 223902 (2014), URL https://link.aps.org/doi/10.1103/PhysRevLett.112.223902.

[46] J. Kasparian, R. Sauerbrey, and S. Chin, Applied Physics B **71**, 877 (2000), URL https://doi.org/10.1007/s003400000463.

[47] A. Becker, N. Aközbek, K. Vijayalakshmi, E. Oral, C. M. Bowden, and S. Chin, Applied Physics B **73**, 287 (2001), URL https://doi.org/10.1007/s003400100637.

[48] A. Janicek, E. Thornton, T. Garrett, A. Englesbe, J. Elle, and A. Schmitt-Sody, IEEE Trans. Plasma Sci. **48**, 1979 (2020).

[49] J. Wymer, J. Elle, E. Ruden, A. Englesbe, and A. Lucero, in *60th Annual Meeting of the APS Division of Plasma Physics* (2018).

[50] E. W. Rosenthal, N. Jhajj, I. Larkin, S. Zahedpour, J. K. Wahlstrand, and H. M. Milchberg, Optics Letters **41**, 3908 (2016), URL http://ol.osa.org/abstract.cfm?URI=ol-41-16-3908.

DISTRIBUTION LIST

DTIC/OCP
8725 John J. Kingman Rd, Suite 0944
Ft Belvoir, VA 22060-6218 1 cy

AFRL/RVIL
Kirtland AFB, NM 87117-5776 1 cy

Official Record Copy
AFRL/RDHP/Andreas Schmitt-Sody 1 cy